Daniele Massini[1]
DIEF—Department of Industrial Engineering,
University of Florence,
Via di Santa Marta 3,
Florence 50139, Italy
e-mail: daniele.massini@htc.de.unifi.it

Emanuele Burberi
DIEF—Department of Industrial Engineering,
University of Florence,
Via di Santa Marta 3,
Florence 50139, Italy

Carlo Carcasci
DIEF—Department of Industrial Engineering,
University of Florence,
Via di Santa Marta 3,
Florence 50139, Italy

Lorenzo Cocchi
DIEF—Department of Industrial Engineering,
University of Florence,
Via di Santa Marta 3,
Florence 50139, Italy

Bruno Facchini
DIEF—Department of Industrial Engineering,
University of Florence,
Via di Santa Marta 3,
Florence 50139, Italy

Alessandro Armellini
Polytechnical Department of Engineering
and Architecture,
University of Udine,
Via delle Scienze 206,
Udine 33100, Italy

Luca Casarsa
Polytechnical Department of Engineering
and Architecture,
University of Udine,
Via delle Scienze 206,
Udine 33100, Italy

Luca Furlani
Polytechnical Department of Engineering
and Architecture,
University of Udine,
Via delle Scienze 206,
Udine 33100, Italy

Effect of Rotation on a Gas Turbine Blade Internal Cooling System: Experimental Investigation

A detailed aerothermal characterization of an advanced leading edge (LE) cooling system has been performed by means of experimental measurements. Heat transfer coefficient distribution has been evaluated exploiting a steady-state technique using thermochromic liquid crystals (TLCs), while flow field has been investigated by means of particle image velocimetry (PIV). The geometry key features are the multiple impinging jets and the four rows of coolant extraction holes, and their mass flow rate distribution is representative of real engine working conditions. Tests have been performed in both static and rotating conditions, replicating a typical range of jet Reynolds number (Re_j), from 10,000 to 40,000, and rotation number (Ro_j) up to 0.05. Different crossflow conditions (CR) have been used to simulate the three main blade regions (i.e., tip, mid, and hub). The aerothermal field turned out to be rather complex, but a good agreement between heat transfer coefficient and flow field measurement has been found. In particular, jet bending strongly depends on crossflow intensity, while rotation has a weak effect on both jet velocity core and area-averaged Nusselt number. Rotational effects increase for the lower crossflow tests. Heat transfer pattern shape has been found to be substantially Reynolds independent. [DOI: 10.1115/1.4036576]

Introduction

In order to achieve higher thermal efficiency and power output of a gas turbine, a key parameter is the increase of turbine inlet temperature (TIT). A drawback of this trend is that high heat loads can occur and have to be managed by means of highly efficient cooling systems in order to ensure components safety. The blades' LE is one of the most thermally stressed parts and needs to be deeply studied during the design process. A widely used cooling technique for such region consists of a multiple jets system generated by a radial feeding channel (cold bridge) impinging on the leading edge internal surface. Several phenomena affect heat transfer in this region such as jet impingement itself, coolant extraction, and convection over those surfaces not directly impacted by the jets [1].

The cooling system can be described by different geometrical parameters such as leading edge sharpness, travel distance from the jet nozzles to the leading edge surface, and extraction holes distribution (number, location, angle). The flow field generated inside the LE can be characterized by the jet Reynolds number

$$\mathrm{Re}_j = \frac{U_j \cdot D_h \cdot \rho}{\mu} \tag{1}$$

[1]Corresponding author.

Contributed by the Heat Transfer Committee of ASME for publication in the Journal of Engineering for Gas Turbines and Power. Manuscript received February 22, 2017; final manuscript received March 29, 2017; published online June 1, 2017. Editor: David Wisler.

and, in rotating blades, by the rotation number

$$\mathrm{Ro}_j = \frac{\Omega \cdot D_h}{U_j} \tag{2}$$

The interaction between jet and LE geometry is responsible for a particular flow field which affects heat transfer performances: for this reason, it is of primary importance to experimentally replicate both actual geometrical and boundary conditions.

Pioneering works on impingement cooling systems were carried out by many researchers: Metzger et al. [2,3], Kercher and Tabakoff [4], Martin [5], Florschuetz et al. [6,7], and Behbahani and Goldstein [8]. These authors investigated convective heat transfer on a flat target surface under an array of impingement jets. Many parameters such as recovery factor, effectiveness, and heat transfer coefficient for different nozzle-to-plate distances, Reynolds numbers, and temperature differences were considered and linked with the local heat transfer enhancement.

A step further toward leading edge internal impingement was done by Chupp et al. [9], Metzger et al. [10], and Hrycak [11], which considered a concave target surface for impingement jets. In particular, Metzger et al. [10] suggested that for sharp surfaces the jets could impinge first on the side walls of the cavity, thus generating a heat transfer pattern significantly different from the one obtained for a flat surface.

More recent works of Bunker and Metzger [12] expressly focused on the impingement cooling of turbine blade leading edge region: they studied the effect of impingement jet holes spacing, jet-to-target spacing, leading edge radius of curvature, and jet Reynolds number. Their work suggested Re_j to be the main driving parameter for heat transfer in a cold bridge system, with a weaker influence of coolant extraction configuration.

The effects of the leading edge internal geometry and the boundary conditions, such as coolant extraction for external cooling systems or internal and external crossflow, were studied by Taslim et al. [13,14], Taslim and Bethka [15], and Elebiary and Taslim [16]. An important finding of such investigations was that heat transfer rate is strongly enhanced by the presence of extraction holes and of turbulence promoters.

All of these considerations found confirmation in recent experimental and numerical investigations performed by Andrei et al. [17] and Facchini et al. [18] at the University of Florence: different leading edge geometries and impingement plates were tested, reproducing actual engine jet Reynolds number conditions and the effect of asymmetric coolant extraction between pressure side (PS) and suction side (SS). All of the aforementioned studies were performed in steady conditions, but recently many researchers have focused on the heat transfer evolution in rotating conditions: Iacovides et al. [19], Craft et al. [20,21], Hong et al. [22–24], and Deng et al. [25]. All of these works report that heat transfer is negatively affected by rotation. On the contrary, Jung et al. [26] found a heat transfer enhancement for small jet-to-target surface distances and if crossflow and Coriolis force induce opposite jet deflections.

This controversy about the effect of rotation on jet impingement heat transfer cannot find a simple solution, since boundary conditions have a direct impact on jet generation. For this reason, it is of primary importance to reproduce the whole admission and extraction systems of the cooling geometry.

A novel rotating test rig was developed with the goal of reproducing a turbine leading edge section equipped with a cold bridge system. The geometry presents three impingement holes and four rows of coolant extraction holes, two for shower head (SH) and two for film cooling (FC). Realistic boundary conditions were provided, such as rotating feeding channel and differential coolant extraction between suction and pressure side due to blade external pressure distribution. Experimental investigations on heat transfer on the impingement target surface (through TLCs) and on flow field inside the LE cavity (through PIV measurements) helped to evaluate the effect of rotation at different working conditions, outlining the importance of feeding channel pressure distribution on jet generation. Static heat transfer measurements were compared with published experimental data and correlations, in order to provide measurement technique and postprocessing validation.

Experimental Facility

Leading Edge Model. The investigated model is a scaled up (scale factor (SF) = 30) turbine blade leading edge geometry, based on an innovative cold bridge impingement cooling system. As depicted in the sectional view in Fig. 1, the cooling air enters a trapezoidal feeding channel at its inner radial extremity, and a part of it enters three holes located on an impingement plate and generates three jets, which impact on the LE internal surface. The mass flow not entering the impingement holes is extracted from the model at the radial outer extremity of the feeding channel.

Impingement plate is 30.1 mm thick and houses three large racetrack shaped holes with an exit hydraulic diameter $D_h = 35.5$ mm, $l/D_h = 0.85$, and a radialwise spacing $P_x = 133.5$ mm. The external geometry replicates in enlarged scale the leading edge of a high pressure airfoil: the main dimensionless parameters are $Z/D_h = 2.34$, $P_x/D_h = 3.75$, and the target plate curvature $D_{\mathrm{LE}}/D_h = 1.11$. The axis of the model central jet is located at a radius of 750 mm. Four large ribs confine the jet impact locations. The spent coolant is extracted from the impingement cavity by four rows of holes, two for film cooling (FC) and two for shower head (SH), composed of six holes each. The model is made of transparent polymethyl methacrylate (PMMA), in order to obtain both complete optical access to the inner geometry and thermal insulation.

Test Rig. The experimental survey presented in this paper was conducted exploiting two similar test rigs presenting few peculiarities in order to perform heat transfer characterization or flow visualization on rotating internal channels.

Heat transfer coefficient evaluation was conducted on the facility located at the Industrial Engineering Department of the University of Florence, a scheme of which is reported in Fig. 2. The

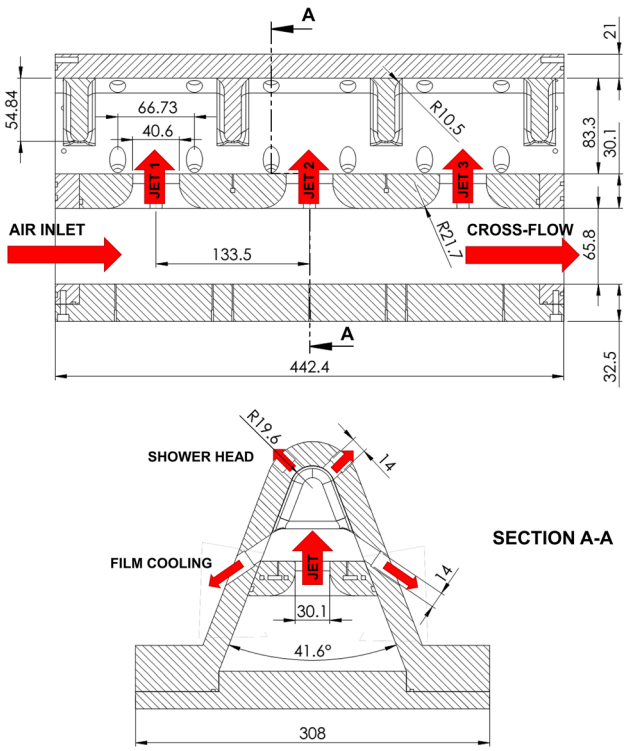

Fig. 1 Sectional view of LE model. Measures are in mm.

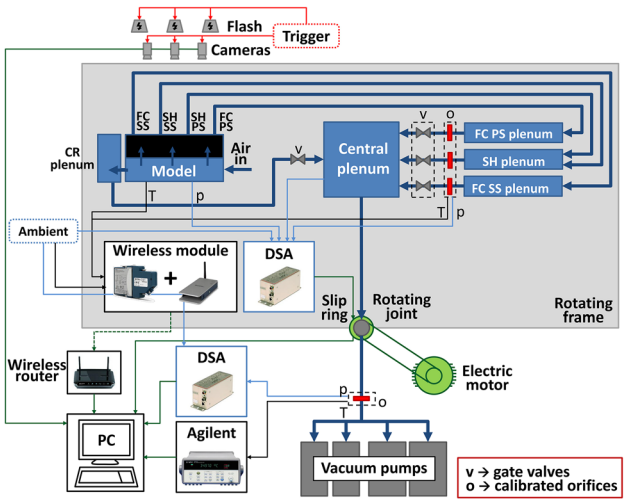

Fig. 2 Test rig scheme

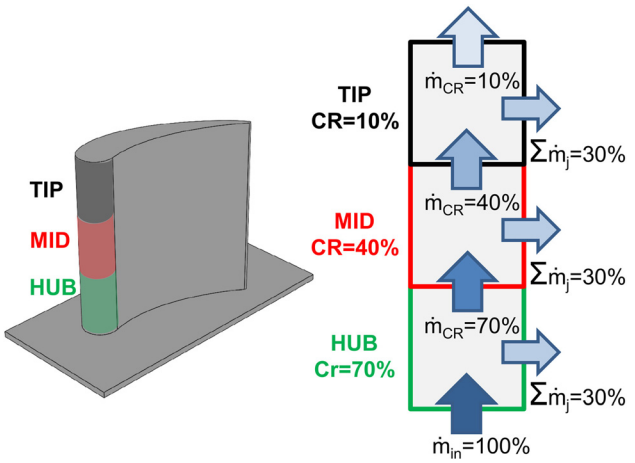

Fig. 4 Crossflow scheme

rig consists of an open loop suction type wind tunnel, installed on a rotating chassis designed by Bonanni et al. [27] (Fig. 3). A rotary joint allows air to be drawn from the test section and several slip rings ensure data transfer and onboard instrumentation power supply. An inverter-controlled electric motor (Marelli, IP55 7.5 kW three-phase-asynchronous—inverter Lenze 7.5 kW 400 V IP21), located under the joint, enables the rotation thanks to a transmission belt. The vacuum system allows air to be drawn from the rig and is composed by four rotary vanes vacuum pumps, two with a capacity of 900 m^3/h each and two with 300 m^3/h each. The model described in the Leading Edge Model section is installed on an arm of the rotating chassis. An inlet section provides air at ambient conditions to the model and houses a filter and a flow-straightener. Coolant flow then evolves into the model and is extracted through the crossflow channel outlet and the four extraction holes rows (FC and SH). Such rows are connected to three different plena, one for each film cooling row and the other for the two shower head rows, symmetrically placed on the other side of the rotating chassis. Each extraction hole is connected to a corresponding hole on the plenum through a flexible duct, and these holes are located at the same radius, with the aim to compensate radial pumping effect during rotation. Each plenum is equipped with an experimentally calibrated orifice and a gate valve, allowing a fine mass flow regulation. This solution allows to impose a differential mass flow extraction between the pressure side (PS) and the suction side (SS), thus simulating the effect of the external pressure distribution: 50% of the coolant air is extracted from the two rows of SH holes, 10% from the PS film cooling holes and the remaining 40% from the SS film cooling holes.

Another gate valve is placed at the feeding channel outlet so that it is possible to vary the ratio between the crossflow and the jets mass flow rate: this allows the reproduction of different portions of the blade through the same model, as depicted in the scheme in Fig. 4. In particular, three portions were investigated, corresponding to hub, midspan, and tip blade sections: the mass flow rate leaving the model through the feeding channel exit is used to identify such conditions and is set equal to 70% (HUB), 40% (MID), and 10% (TIP) of the total coolant flow entering the blade.

The different flows from the extraction holes plena and the feeding channel outlet are then collected in a single central plenum, from which the overall air mass flow is extracted and measured using a downstream orifice according to the standard EN ISO 5167-1.

The flow temperature is measured in different locations with several T-type thermocouples connected to a NI 9214 16-channel isothermal input module, with three cold junction compensation sensors to provide the thermocouples an absolute temperature reference value: in such way, the manufacturer declares a module

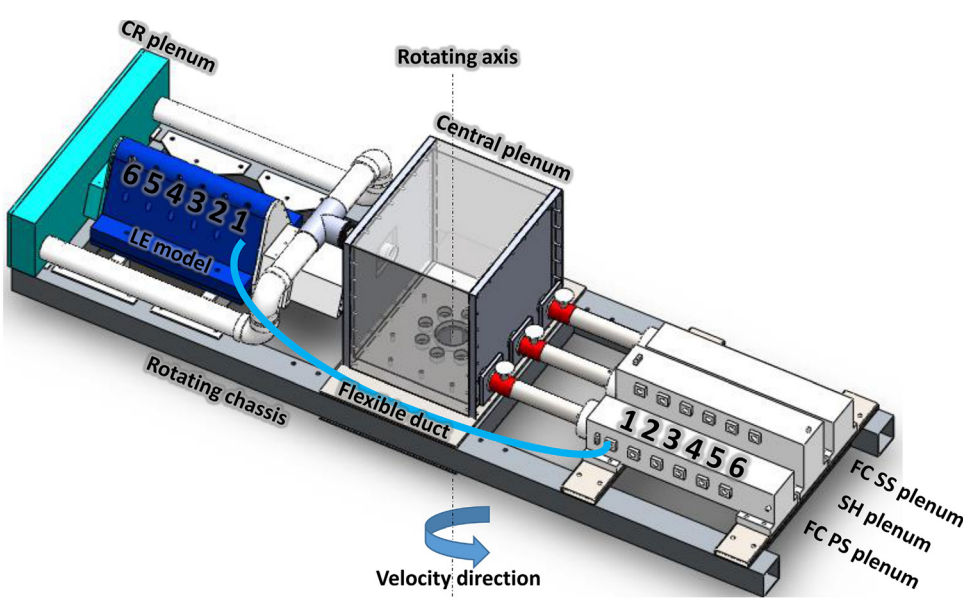

Fig. 3 Rotating test rig

measurement accuracy of 0.37 K in the current operating conditions. The module is linked to a NI cDAQ-9191 Wi-Fi chassis, which allows wireless temperature data transmission and recording in both static and rotating conditions. The whole assembly is installed on a dedicated support on the rotating chassis. More thermocouples are located outside the test rig and are linked to a data acquisition/switch unit (Agilent 34970A) with a measurement accuracy of 0.5 K.

Two pressure scanners Scanivalve DSA 3217 with temperature compensated piezoresistive relative pressure sensors, 16 channels each and a maximum accuracy of 6.9 Pa, are used: one is installed inside the central plenum, allowing onboard measurements of static pressure as well as of mass flow rate through the three onboard orifices; the other is located outside the rig and is used to meter the pressure drop across the downstream orifice.

An equivalent test rig is located at the Turbomachinery and Energy System Laboratory at University of Udine with the goal of performing flow field measurement exploiting PIV technique.

The rig allows to replicate actual engines working conditions in terms of both jet Reynolds and rotation numbers, which can be varied up to $Re_j = 40{,}000$ and $Ro_j = 0.05$. The reduced temperature differences of coolant air across the model allow to neglect any buoyancy effect. Given the model scaling, the investigated conditions correspond to a maximum mass flow rate of 0.165 kg/s and a maximum rotational speed of 170 rpm for the $Re_j = 30{,}000$, $Ro_j = 0.05$, CR = 70% test.

Heat Transfer Measurement Technique. Heat transfer evaluation was performed exploiting a steady-state technique, which consists on the imposition of a known heat flux to the heat transfer surface. Energy conservation provides the following definition of convective heat transfer coefficient:

$$h = \frac{\dot{q}_{\text{conv}}}{T_w - T_c} = \frac{\dot{q}_{\text{gen}} - \dot{q}_{\text{loss}}}{T_w - T_c} \tag{3}$$

where $\dot{q}_{\text{conv}}$ is the convective heat flux, $\dot{q}_{\text{gen}}$ is the imposed generated heat flux, $\dot{q}_{\text{loss}}$ is the portion of heat flux not exchanged through convection, T_w is the wall temperature, and T_c the coolant temperature. T_c is obtained as the average of the three jet temperatures, measured by T-type thermocouples, which were verified to have differences within the sensor uncertainty. Temperature measurement on the impingement target surface is achieved through Hallcrest 30C20W wide band thermochromic liquid crystals with an activation band between 30 and 50 °C. TLC activation range was chosen to ensure TLCs to be colored, and thus measurement to be performable, on the whole measurement surface in every test condition.

Before the experiments, a robust TLC color–temperature response calibration was performed to achieve high accuracy measurements, according to the steady-state gradient method [28]. Calibration and heat transfer tests were performed with identical optical conditions, and the insensitivity of color–temperature response was verified in the applied range of viewing angles. Given the high curvature of the LE geometry, a set of three Sony XCD-SX90CR cameras and Dörr DE 500 W studio flashes have been used for images acquisition: two cameras were dedicated to the lateral flat surfaces, while the third focuses on the leading edge region, thus reducing the viewing angles with respect to the investigated surface. The whole system is synchronized by a custom built electronic circuit triggered by a laser transducer.

A constant heat flux is obtained through an electrically heated 25.4-μm-thick Inconel Alloy 600 sheet, applied on LE internal surface and supplied by two copper bus bars. Electric current across Inconel is provided by a DC power supply Agilent N5700.

Considering the complex geometry investigated, the Joule heat flux does not have a constant distribution; moreover, the heat flux which is not exchanged by convection $\dot{q}_{\text{loss}}$ needs to be quantified for h calculation (Eq. (3)). For this reason, a thermal-electric finite element method (FEM) analysis is performed by exploiting ANSYS Mechanical APDL® v15. The FEM model includes both the Inconel heater and the PMMA test article, and considers heat transfer due to convection at the external surface and inside the extraction holes thanks to suitable correlations. Since conductive heat fluxes inside the model depend on the heat transfer coefficient distribution, an iterative procedure is required: in the first step, a first attempt h distribution is calculated considering a constant heat flux and imposed as a boundary condition for the simulation. The result is then more realistic Joule generated $\dot{q}_{\text{gen}}$ and dispersed $\dot{q}_{\text{loss}}$ heat fluxes distributions, which allow a more accurate h pattern to be calculated and the simulation to be iterated using the latter as a boundary condition. This process is repeated until convergence. In the present case, the amount of dispersed heat varies between 5% and 15% of the Joule generated power. The whole measurement technique and postprocessing is deeply described in Ref. [29].

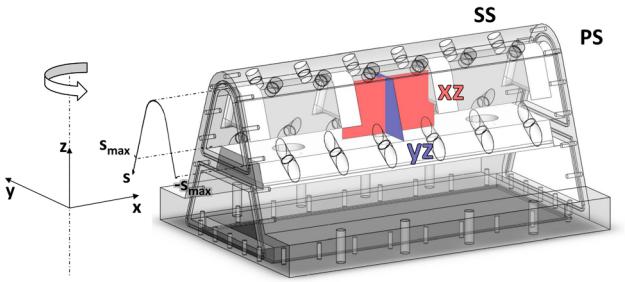

Fig. 5 PIV reference system and investigated planes

PIV Measurement Technique. Flow field measurements were performed by means of 2D and stereo-PIV techniques. The PIV system is custom-made and features a 200 mJ double cavity Nd-YAG pulsated laser from Litron Lasers Ltd. (Rugby, UK) and two Sensicam cameras from PCO AG (Kelheim, Germany) with cooled 12 bit CCD with a resolution of 1024 × 1280 pixels. Cameras mount Nikkor optics from Nikon (Tokyo, Japan) with either 105, 60, or 35 mm fixed focal length and two-axis Scheimpflug

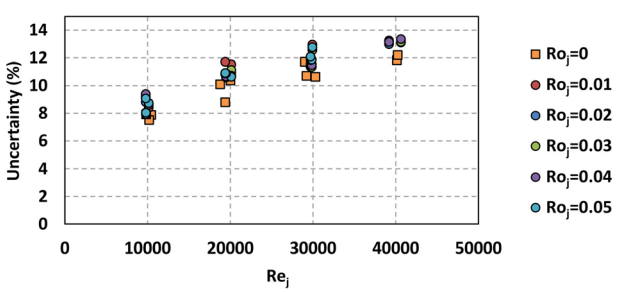

Fig. 6 Average heat transfer coefficient uncertainty for the whole test matrix

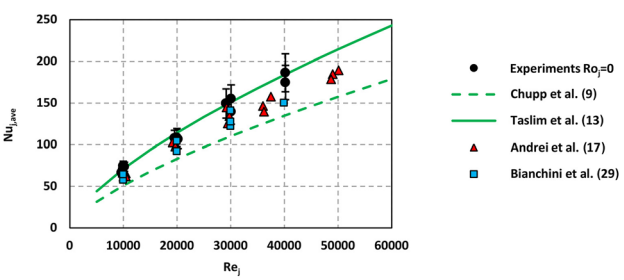

Fig. 7 Average Nusselt results in static conditions

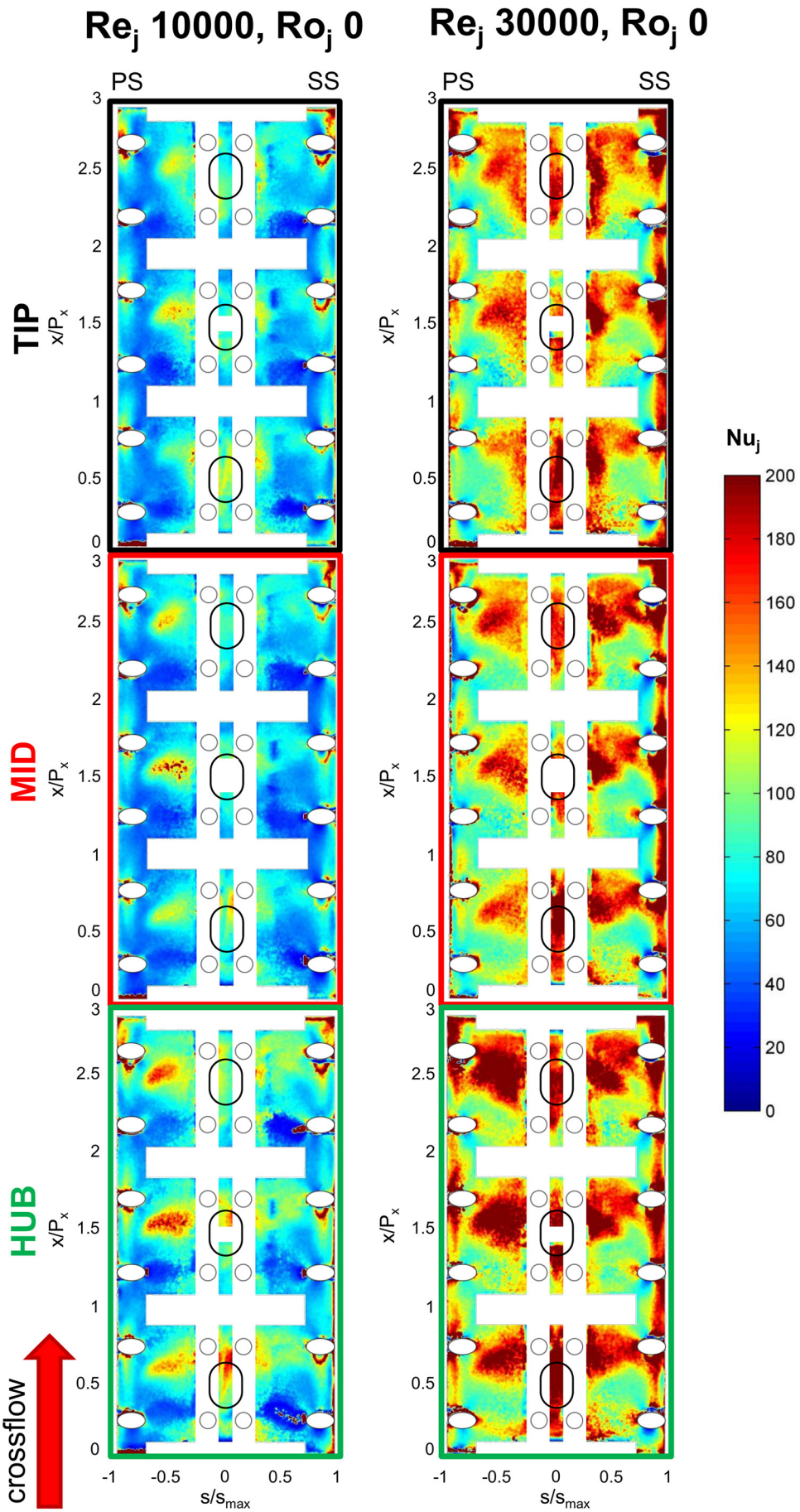

Fig. 8 2D Nu$_j$ distribution for a whole blade configuration at Re$_j$ = 10,000, Ro$_j$ = 0 and Re$_j$ = 30,000, Ro$_j$ = 0

adapters for stereo viewing. Cameras and laser are connected through the synchronization and acquisition systems. The seeding was provided by a Laskin-nozzle-type seeding generator operated with vegetable oil, which guarantees a very narrow particle size distribution with an average diameter of 1.2 μm.

For both 2D and stereo-PIV data, the commercial software PIV VIEW (PIVTEC Gmbh, Göttingen, Germany) was used to perform the processing of the image pairs. In particular, for stereo-PIV data, image back-projection and then stereo reconstruction were computed; furthermore, a disparity correction was also used in order to minimize the misalignment errors [30].

Concerning the measurements under rotation, it has to be underlined that the present PIV system is stationary; therefore, a phased-locked configuration has been adopted. Since the measurement output is the absolute velocity field, a more complex pre- and postprocessing procedures [31,32] were adopted in order to get an accurate reconstruction of the relative velocity field inside the test section.

Detailed description of the investigated planes in the PIV experimental campaign, as well as validation of the rotating and stereo-PIV tests, can be found in Ref. [33]. In order to have a deep understanding of the impingement jets evolution, the two planes shown in Fig. 5 were chosen for the PIV measurements. The reference system has origin in the rotating axis in the model symmetry plane, and the z-axis is centered on the impingement plate side facing the LE cavity.

Experimental Uncertainty

TLC Uncertainty. Experimental uncertainty on the heat transfer coefficient evaluation was performed locally, for every measured point, according to the standard ANSI/ASME PTC 19.1 [34], based on the Kline and McClintock method [35]. Among the measured variables considered in the calculation, the leading parameter for uncertainty increase was found to be the difference between coolant and wall temperatures. For this reason, the maximum uncertainty is verified in the jet impact regions, where the temperature difference between the wall and the fluid is smaller than any other point on the investigated area. The maximum local uncertainty in these regions, found for tests performed at $\mathrm{Re}_j = 40{,}000$, was of around 20% for static tests, while for rotating tests it raised to around 30% given the lower accuracy of onboard cold junction compensation. Nevertheless, far from jet impact zones the uncertainty is usually under 10%, resulting in average values always lower than 13% and 14% for static and rotating tests, respectively.

An overview of the average uncertainties for every test performed is reported in its evolution with Re_j in Fig. 6.

PIV Uncertainty. The results that will be presented refer only to statistical quantities, such as the time-averaged velocity fields. Due to the limited number of samples (1000) used to compute the flow statistics, the sampling error tends to be larger than other error sources and therefore it was chosen as the overall upper bound estimate for the PIV data uncertainty.

For the 2D measurement under static conditions, the normalized r.m.s. errors in the statistical quantities are computed as in Ref. [36]

$$\epsilon_U = \frac{\sigma[U]}{|U|} = \frac{1}{\sqrt{N}} \cdot \frac{u'}{|U|}, \quad \varepsilon'_u = \frac{\sigma[u']}{u'} = \frac{1}{\sqrt{2N}} \tag{4}$$

where σ is the standard deviation, U is the mean velocity, u' is the r.m.s. velocity fluctuation, and N is the number of independent samples. The uncertainties in the measured values of U and u' are simply obtained by multiplying the errors in Eq. (4) by a confidence coefficient, Z_c. Assuming values $Z_c = 1.96$ (corresponding to a 95% confidence level) and $N = 1000$, the overall upper bound estimate of the uncertainty in the mean velocities turns out to be less than 2%. This value applies to the largest part of the velocity fields, with the exception of those limited regions affected by very low velocities and high fluctuations, namely inside zones of separated flow. Under the same assumptions, the maximum uncertainty in the estimate of the r.m.s. velocities is less than 5%.

For the data acquired under rotation, error introduced by the image processing has to be taken into account. In accordance with the analysis proposed by Armellini et al. [32], the velocity uncertainty must be increased by 1% of U_b (Eq. (5)). As far as concern stereo-PIV measurements accuracy, it has been quantified through a cross comparison with the 2D PIV data in both static and rotating conditions.

Experimental Results

The present work focuses on the performance of the cold bridge system in terms of convective heat transfer with the coolant flow: for this reason, the results are expressed in terms of jet Nusselt number ($\mathrm{Nu}_j = hD_h/k$). A test matrix of 64 points was performed: Re_j was varied with steps of 10,000 and rotation with steps of 0.01; moreover, for each Re_j–Ro_j couple, the three crossflow conditions (HUB, MID and TIP) were tested. Given the high mass flow rate and rotational speed required, cases at $\mathrm{Ro}_j = 0.05$ and 70% crossflow were limited to a maximum $\mathrm{Re}_j = 30{,}000$. Few test cases, representative of all the configurations tested, will be shown in terms of 2D Nusselt number distributions and PIV velocity plots in order to better understand the phenomena driving the jet generation.

For a better representation, Nu_j distribution on the inner curved surface was reported to a flat plane rolling out the LE geometry. On such flattened surface, horizontal coordinate s represents the circumferential distance from the leading edge center along the surface and is scaled with respect to the maximum lateral extension $s_{\max}$; instead, vertical coordinate x indicates the radial

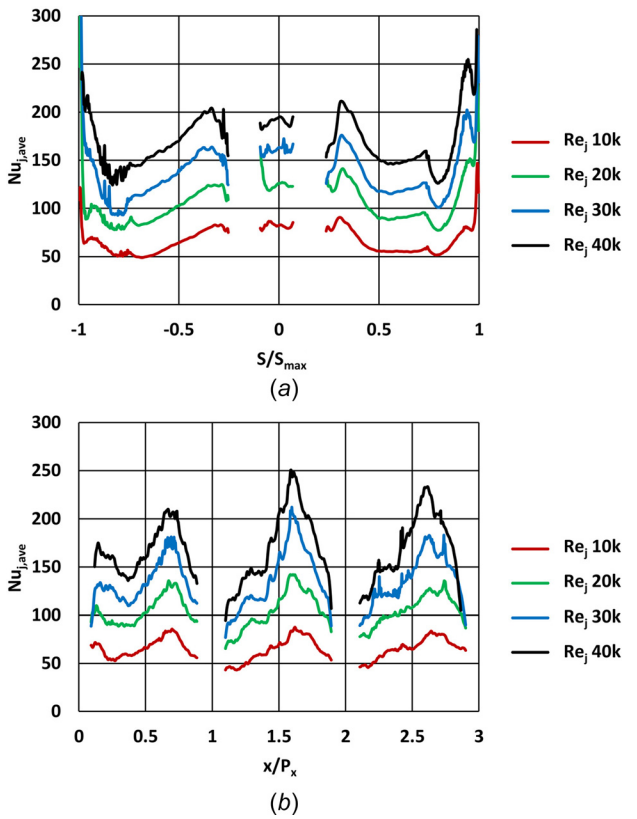

Fig. 9 $\mathrm{Nu}_{j,\mathrm{ave}}$ distribution comparison for different Re_j in TIP condition: (*a*) $\mathrm{Nu}_{j,\mathrm{ave}}$ circumferential distribution and (*b*) $\mathrm{Nu}_{j,\mathrm{ave}}$ radial distribution

distance from the inner point of the measurement surface and is scaled with the impingement holes radial pitch P_x.

The areas corresponding to the ribs and to the glued parts of the geometry are removed from the analysis, because of the constraints implied by both the geometry and the measurement technique. The extraction holes and the projection of the impingement hole position are also represented in the maps.

Static Conditions. Static tests were performed in order to provide a "zero" condition against rotating tests, as well as to provide a measurement technique validation by means of a comparison with the results obtained from similar LE models found in open literature.

Overall area-averaged $Nu_{j,ave}$ measured in static conditions, together with the relative uncertainty, are summarized in the graph in Fig. 7, which underlines the good agreement with various test cases found in literature [9,13,17] and with a Reynolds-averaged Navier–Stokes (RANS) computational fluid dynamics (CFD) investigation performed by Bianchini et al. on the present model and already presented in Ref. [29].

Figure 8 shows a first comparison of two different working conditions: $Re_j = 10{,}000$ and 30,000.

The Nusselt peaks reveal the presence of the jets impinging on the internal surface: there are three regions presenting higher Nusselt values, one in the center of the LE and two on the lateral surfaces. Figure 8 also reveals the effect of crossflow on Nu_j distribution, and consequently on the jet flow field: the shape of high Nu_j areas changes moving from HUB to TIP, revealing a different internal flow field. Since the jet mass flow is approximately the same in the various tests and the only difference consists in the crossflow, i.e., the flow providing coolant to the jets, it can be supposed that the variations in Nu_j distribution are due to differences in the jet generation itself. The reported maps also show a displacement between pressure and suction side, probably due to the different mass flow extraction. The influence of extraction holes dimensions, number, and position was studied by Andreini et al. [37], showing that these parameters can only secondarily affect the Nu_j distribution.

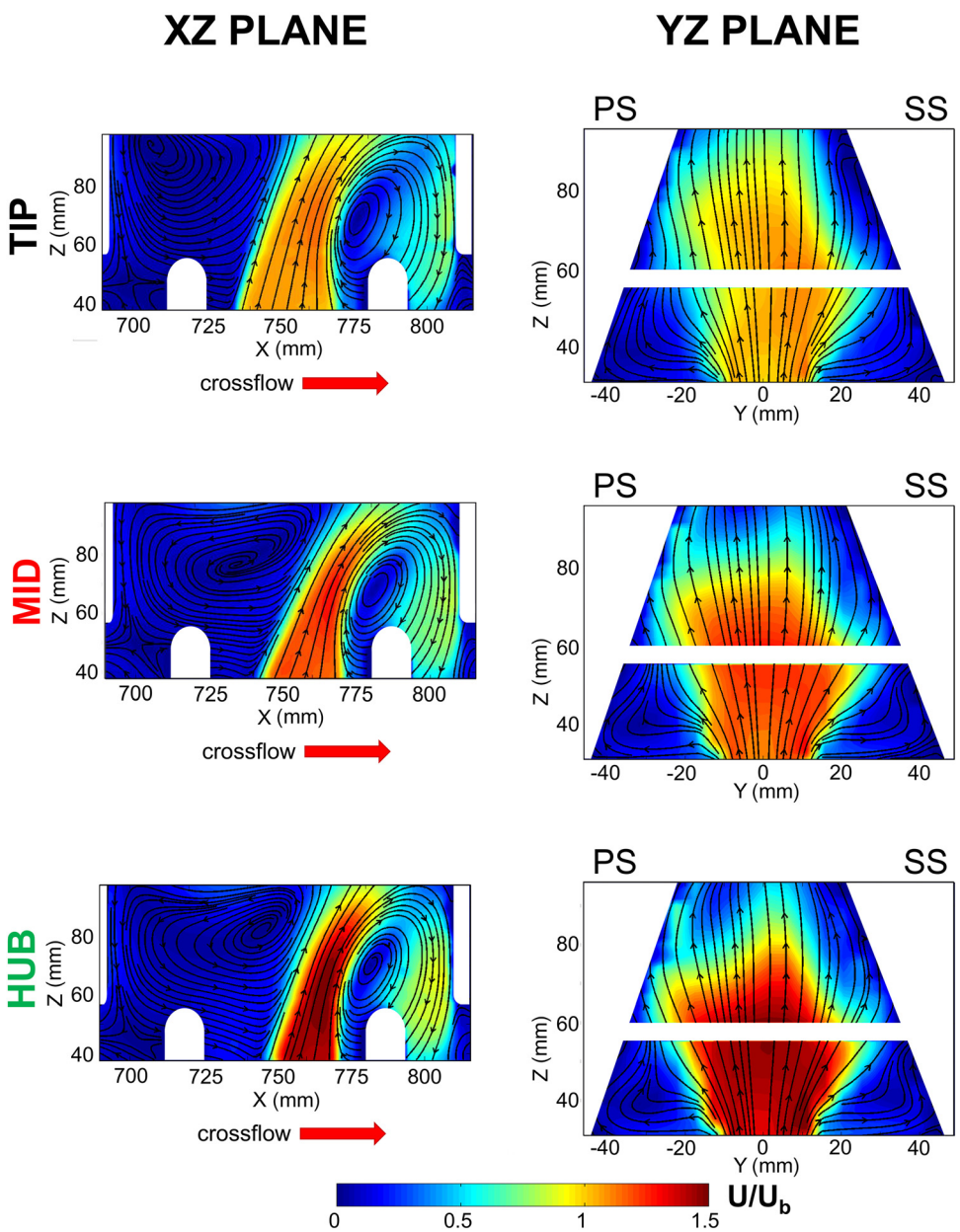

Fig. 10 PIV velocity maps in static conditions for a whole blade configuration at $Re_j = 30{,}000$

A more quantitative comparison is provided in Fig. 9, where experimental results for tests taken in TIP conditions were line-averaged to obtain profiles along circumferential and radial directions.

These results show the effect of Re_j, which is responsible for a high heat transfer increase, even if its distribution seems to remain similar for all the tests. This means that the Re_j does not affect the flow field within the LE cavity. The heat transfer peaks are shifted toward the crossflow direction, suggesting that the heat transfer phenomena are significantly affected by the upstream crossflow conditions.

These experimental evidences find confirmation in PIV measurements, reported in Fig. 10. Velocities are scaled with respect to the jet bulk velocity, defined as

$$U_b = \frac{\mu \mathrm{Re}_j}{\rho D_h} \tag{5}$$

For $Re_j = 30{,}000$, the value of U_b is around 13 m/s for every test.

Observing Fig. 10, the evolution of the jets can be noticed. In the HUB configuration, the mass flow rate leaving the feeding channel is 7/3 of the mass flow rate through the three jets: for this reason, the impingement holes are not able to completely drive the flow normal to the leading edge surface, and the jets migrate toward the ribs. This effect is mitigated going toward the TIP configuration, given the lower crossflow entity. Even so, the jets appear to be significantly bent toward the crossflow direction for every upstream configuration. Another effect of the various crossflow configurations is the spreading of the jets on the lateral surfaces, which is higher for higher feeding channel flow velocities. Moreover, images in the *YZ* planes show a jet displacement toward the pressure side, confirming and explaining the Nu_j distribution.

As already mentioned, the Re_j acts only in an overall mean value variation in terms of both heat transfer and internal flow field. These aspects have been deeply studied by Bianchini et al. [29] and Furlani et al. [33], respectively.

Rotating Conditions. Since a good understanding of the flow field in different blade sections is achieved, the effect of rotation can be analyzed both in terms of heat transfer and internal flow field.

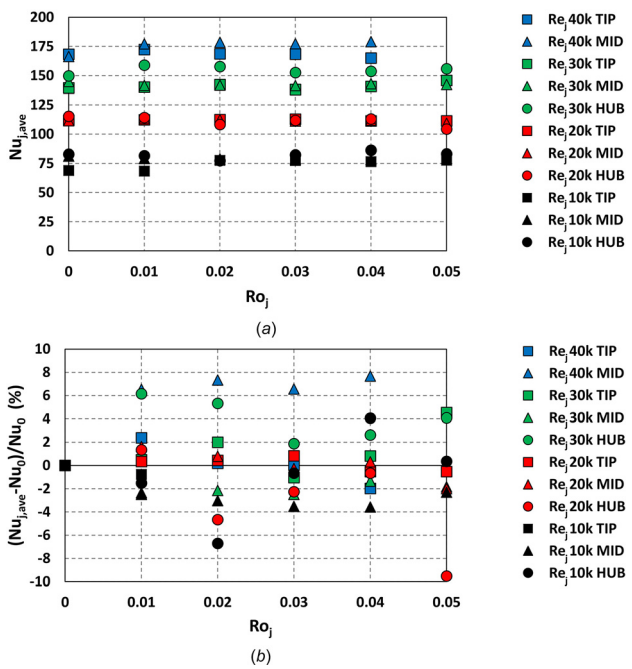

Fig. 11 Average Nu_j variation with Ro_j: (*a*) Effect of rotation on $Nu_{j,ave}$ for all the test points and (*b*) $Nu_{j,ave}$ percentage variation for all the test points

First of all, in order to evaluate the effectiveness of the LE geometry, the average Nusselt number for all the working conditions can be observed. Figure 11(*a*) shows the $Nu_{j,ave}$ evolution for all the test points: again, it is possible to notice the increase with Re_j and the negligible effect of CR on the average heat transfer coefficient for all the test points. Rotation seems to have little effect for this particular geometry, as is better underlined in Fig. 11(*b*): the percentage variation with the respect to the static cases Nu_0 for every Ro_j is comprised of $\pm 8\%$, and a clear trend with Ro_j cannot be identified.

In order to better understand the reason of this fact, it can be useful to consider the Nu_j maps of Fig. 12, where Re_j test at $Ro_j = 0.02$ and $Ro_j = 0.05$ are compared.

These results clearly show that the rotation does not significantly affect Nusselt distribution, even if going from the HUB to the TIP the jets seem to be bended toward the SS. Nu_j maps also show that rotational effects are more and more pronounced as the crossflow mass flow rate decreases. Figure 13 provides a comparison between HUB and TIP conditions at $Re_j = 10$k and 30 k in terms of circumferential distributions of $Nu_{j,ave}$. It shows that tests performed in HUB conditions (CR = 70%) seem to be almost insensitive to rotational effects, while tests performed in TIP configuration (CR = 10%) show a noticeable migration of high Nu_j zones toward the suction sides. Figure 14 clearly shows the jet migration at the blade TIP.

In order to get more information about this phenomenon, the PS and SS Nusselt distributions were separately averaged and their differences evaluated for every Ro_j condition. The results of this analysis are reported in Fig. 15. The differences between PS and SS follow the same trend for similar CR conditions: the HUB is almost insensitive to the rotation; in the MID the differences increase monotonically; and in the TIP, the differences quickly reach a maximum value at $Ro_j = 0.03$ and then start to decrease. Since the Nu_j under an impinging jet is a function of various parameters, such as the jet velocity and the nozzle-to-target surface variation, the maximum trend can be interpreted as consequence of an optimal combination in such parameters. PIV measurements help to understand what happens inside the LE. Figure 16 shows the three CR configurations for $Re_j = 30{,}000$ and $Ro_j = 0.05$: again, HUB and MID seem to be scarcely affected by the rotation, while the jet on TIP is completely rotated toward the SS, thus explaining the higher increase of Nu_j on that side.

Considering the direction of rotation and the main velocity component of the jet, Coriolis forces should not affect the jet itself; nevertheless, the flow velocity in the feeding channel is perpendicular to rotation axis and is thus subject to the generation of a total pressure gradient, positive on the PS, which can cause a jet inclination on the opposite side.

In order to quantify the effect of rotation, velocity profiles were extracted from measurements on the *XZ* plane in HUB and TIP conditions. Figure 17 reports the comparison between static and rotating conditions at the extreme blade span positions (TIP and HUB), the jet is observed close to the racetrack holes and in the middle of the LE cavity: *Z* positions of 40 and 70 mm were indeed chosen in order to highlight the jet evolution. Velocity profiles taken at $Z = 40$ mm present the typical shape of a jet; however, the portion of jet at constant velocity changes passing from HUB to TIP. In HUB condition, the high momentum in *x* direction of the upstream flow causes the impingement jet to flatten toward the hole downstream wall, resulting in a smaller apparent hole section and thus in higher jet velocities. In this case, the rotation alters very little the jet position which is moved forward of 3 mm, maintaining the same shape. The same characteristics are visible at $Z = 70$ mm, where however the jet shape is sharper, due to the dispersion of potential core.

In TIP conditions, the rotation does not cause a jet shift but it ripples the plateau present in static conditions. Moving at $Z = 70$ mm, this effect is amplified and the jet is spread all over the LE cavity.

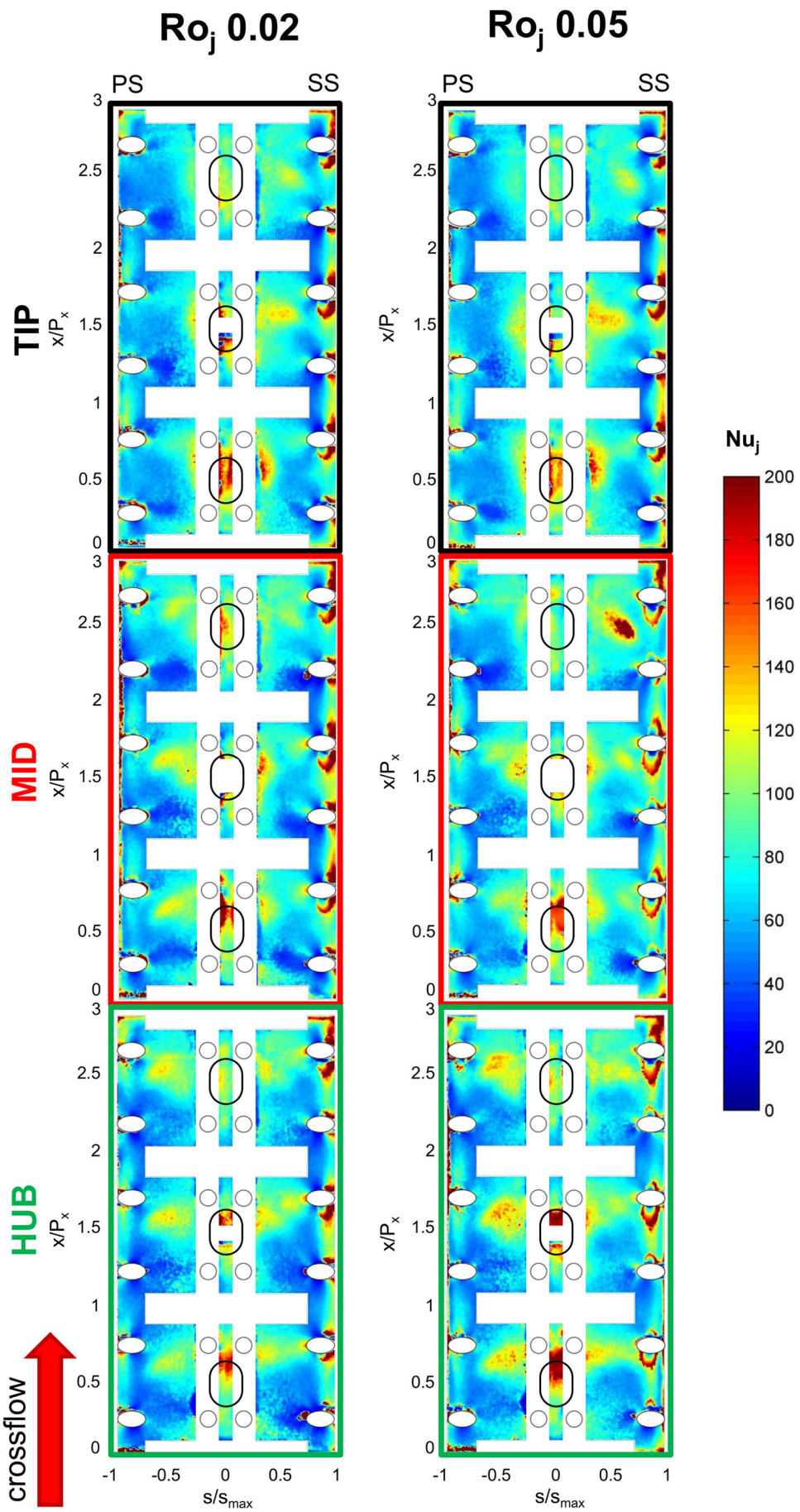

Fig. 12 2D Nu_j distributions at $Re_j = 10{,}000$, $Ro_j = 0.02$ and $Re_j = 10{,}000$, $Ro_j = 0.05$

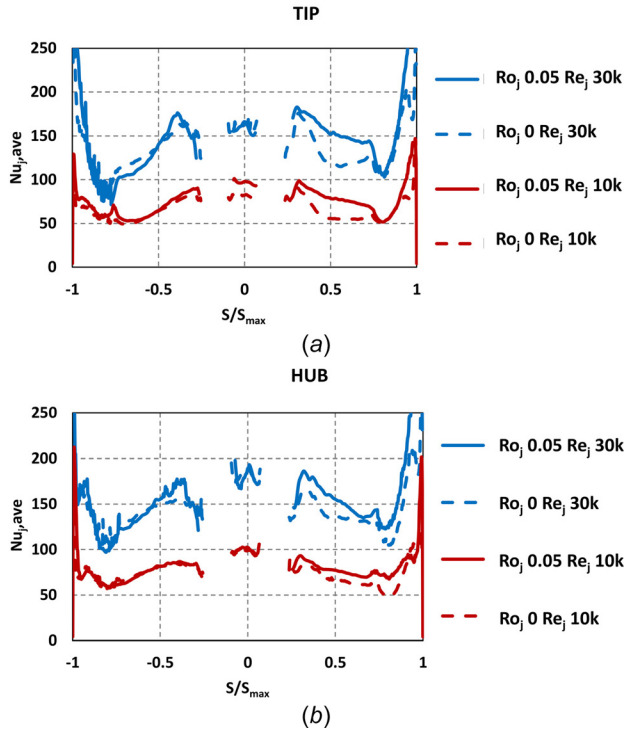

Fig. 13 $Nu_{j,ave}$ circumferential distributions comparison between TIP and HUB conditions: (*a*) $Nu_{j,ave}$ circumferential distribution in TIP conditions and (*b*) $Nu_{j,ave}$ circumferential distribution in HUB conditions

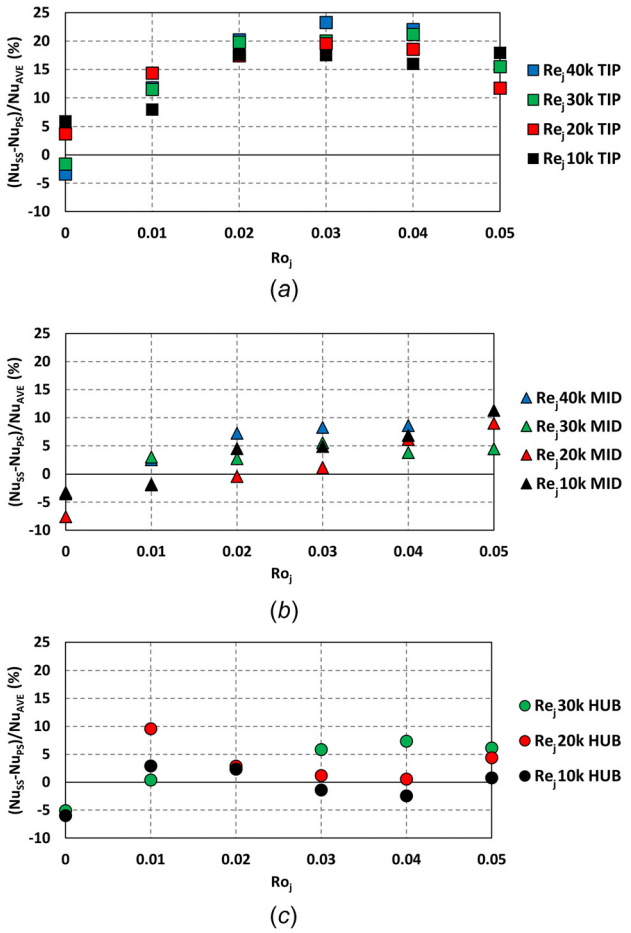

Fig. 15 Nu_j differences between SS and PS at different Ro_j and crossflow conditions: (*a*) TIP, (*b*) MID, and (*c*) HUB

This evidence is confirmed by CFD analysis [38] and also helps to explain the recorded insensitivity of the overall cooling performances to rotation, presented in Fig. 11(*a*), which is in contrast to the open literature results [19–25]. In fact, given the target surface curvature and the impingement holes location, nozzle-to-target surface distance is similar for a wide region of the target area itself: as a consequence, even if rotation causes the jet to bend, nozzle-to-target surface distance not necessarily increases in this case; moreover, the angle between the jet direction and the target surface normal is not drastically altered by a jet inclination (i.e., the jet deflection is not increased): as a consequence, the jet momentum component perpendicular to the solid surface is only slightly altered by the rotation, and heat transfer is almost unaffected by the impact location. Another significant contribution to the heat transfer insensitivity to rotation is given by the ribs, which prevent the formation of a rotation-induced crossflow in the impingement cavity and confine the single jets into a limited region.

Since the jet bending is attributed to Coriolis-induced effects in the feeding channel, this fact can also explain the increased sensitivity to rotation for tests with lower crossflow mass flow rates at a given Ro_j value: in fact, Ro_j is defined with respect to the impingement holes velocity and hydraulic diameter, without considering the feeding channel flow. If a rotation number is defined with respect to the feeding duct ($Ro_{CR} = \Omega \cdot D_{h,CR}/U_{b,CR}$, where $D_{h,CR}$ is the duct hydraulic diameter), it can be noticed that if the crossflow mass flow rate decreases at a given Ro_j value, its bulk velocity $U_{b,CR}$ and Ro_{CR} value increase: as a consequence, it can be supposed that rotational effects on the feeding channel increase as crossflow mass flow rate decreases. Since it has been demonstrated that crossflow has a significant influence on the

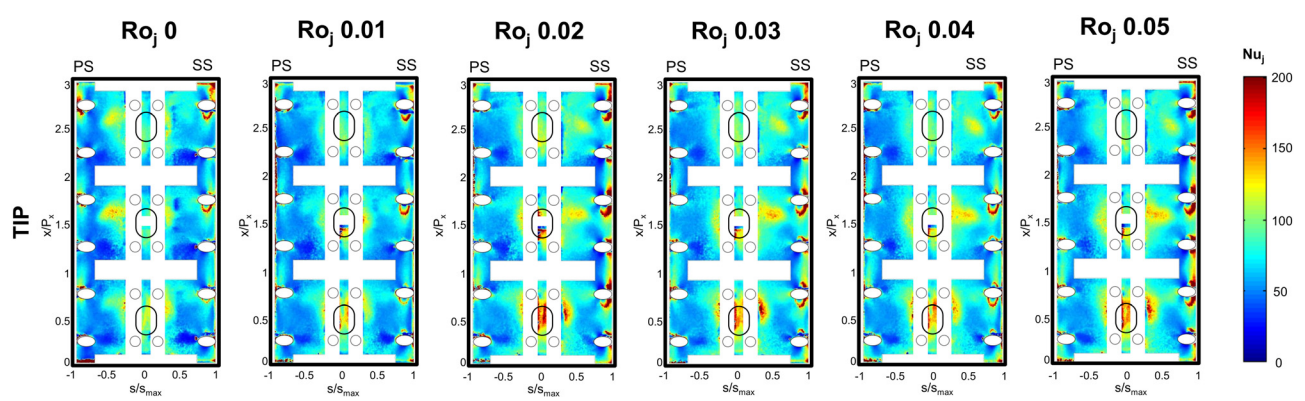

Fig. 14 2D Nu_j distributions at $Re_j = 10{,}000$ and $Ro_j = 00.05$ for the TIP condition

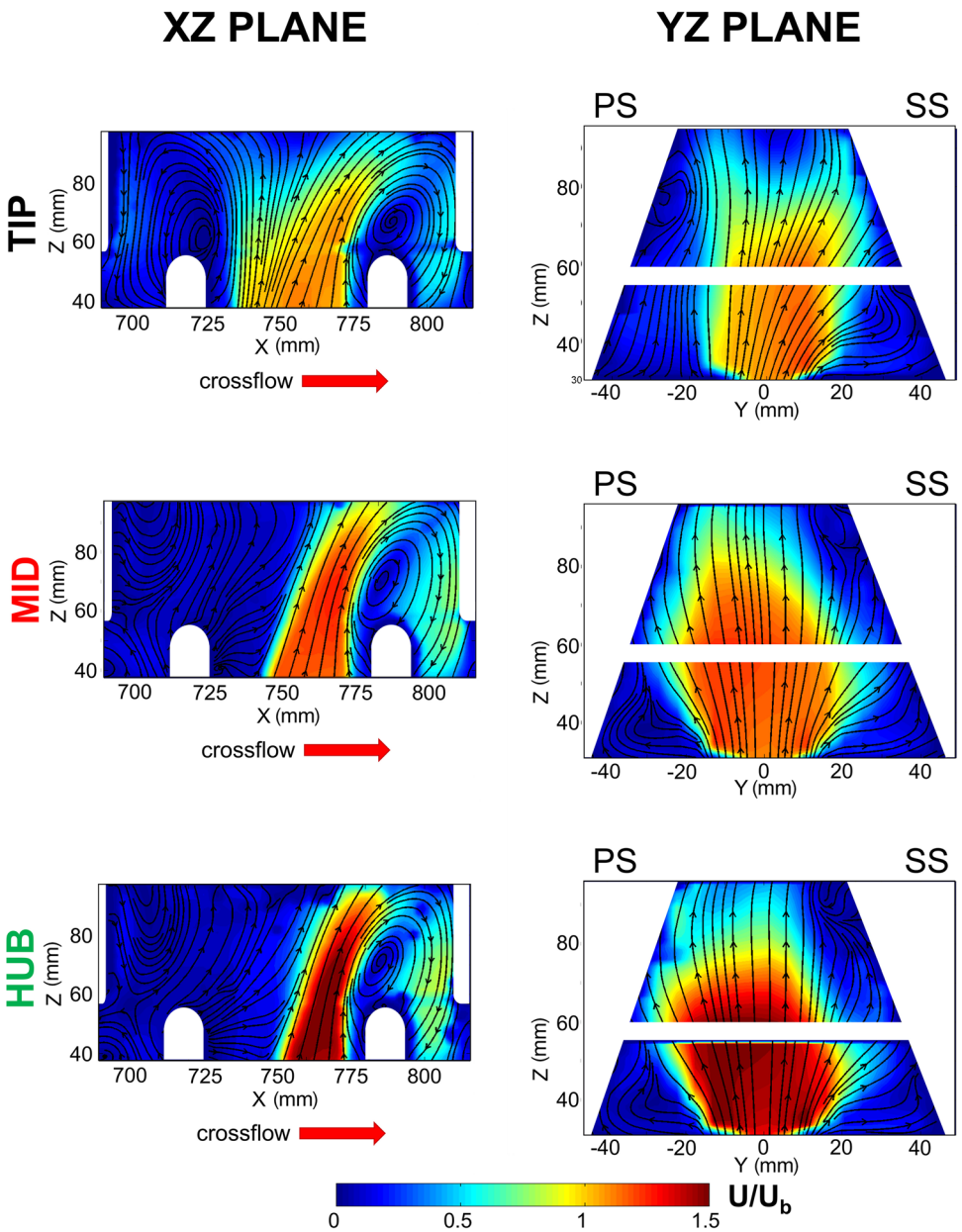

Fig. 16 PIV velocity maps in rotating conditions for a whole blade configuration at $Re_j = 30{,}000$ and $Ro_j = 0.05$

impingement jet generation, it is evident that stronger rotational effects on the feeding channel imply stronger effects on the impingement jet too, i.e., a more pronounced bending. PIV measurements represented in Fig. 16 seem to confirm this supposition.

Conclusions

A turbine leading edge model, equipped with a cold bridge jet impingement cooling system, was tested on two similar rotating test rigs by exploiting different measurement techniques. The goal was to evaluate the heat transfer coefficient distribution on the internal surface by means of TLC steady technique and to characterize the flow field through PIV measurements.

The test rig is able to reproduce actual engine working conditions in terms of jet Reynolds and rotation numbers. Moreover, realistic boundary conditions can be imposed thanks to a fine mass flow split regulation: in such way, typical internal flow field of a blade HUB, MID, and TIP was reproduced, including different feeding channel mass flow rates and differentiated mass flow extraction trough film cooling and shower head holes.

Experimental results were compared in order to link the parameters affecting the generation of the impingement jets with the different Nusselt distributions. By doing so, the following phenomena were identified:

- For every impingement jet, three high Nu_j zones are present, one in the center of the leading edge and the others on the flat side walls; this is due to the shape of the impingement jet, which is bended in the crossflow direction and flattened in the circumferential direction: as a consequence, the jet impacts the side walls as well as the center of the curved surface.
- Higher crossflow values seem to enhance the jet bending and flattening, which results in wider lateral Nu_j peaks.
- Rotation does not significantly alter area-averaged Nu_j values, and its effect on the Nu_j is mainly verified as a shifting of heat transfer peaks toward the suction side; this fact is due to a bending of the jet in this direction, which was

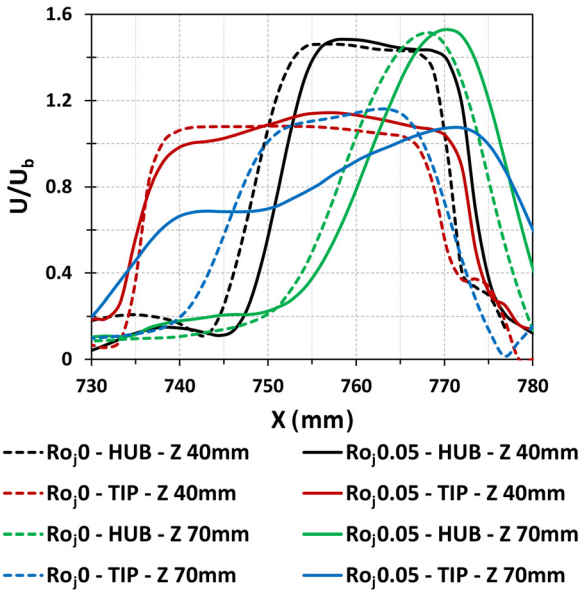

Fig. 17 Velocity profiles for HUB and TIP conditions, effect of rotation at $Re_j = 30{,}000$

interpreted as due to an uneven pressure distribution in the feeding channel.

— Rotational effects on both Nu_j distribution and flow field seem to be more intense as the feeding duct mass flow rate decreases at a given Ro_j value; this can be due to an increase in feeding duct rotation number Ro_c, which corresponds to augmented rotational influences on the impingement jet generation zone and so on the jet itself.

Acknowledgment

The reported work has been supported by the Italian Ministry of Education, University and Research (MIUR).

Nomenclature

D = diameter (m)
h = heat transfer coefficient ($W/m^2 K$)
k = thermal conductivity ($W/m K$)
l = orifice length (m)
N = number of samples
$Nu = (h \cdot D)/k$ = Nusselt number
P = pitch (m)
$\dot{q}$ = heat flux (W/m^2)
r = radius (m)
$Re = (U \cdot D \cdot \rho)/\mu$ = Reynolds number
$Ro = (\Omega \cdot D)/U$ = rotation number
s = circumferential direction (m)
T = temperature (K)
u = velocity fluctuation (m/s)
U = velocity (m/s)
x = radial direction (m)
y = tangential direction (m)
z = axial direction (m)
Z = jet-to-target surface distance (m)
ϵ = error
μ = air dynamic viscosity ($kg/m s$)
ρ = flow density (kg/m^3)
σ = standard deviation
Ω = angular velocity (rad/s)

Subscripts

ave = area-averaged
b = bulk
c = coolant
conv = convection
CR = crossflow
gen = generated
h = hydraulic
j = jet
loss = not exchanged through convection
max = maximum extension
w = wall

Acronyms

CFD = computational fluid dynamics
CR = crossflow
FC = film cooling
FEM = finite element method
LE = leading edge
PIV = particle image velocimetry
PMMA = polymethyl methacrylate
PS = pressure side
RANS = Reynolds-averaged Navier–Stokes
SF = scale factor
SH = shower head
SS = suction side
TIT = turbine inlet temperature
TLC = thermochromic liquid crystal

References

[1] Metzger, D., and Bunker, R., 1990, "Local Heat Transfer in Internally Cooled Turbine Airfoil Leading Edge Regions: Part II—Impingement Cooling With Film Coolant Extraction," ASME J. Turbomach., **112**(3), pp. 459–466.
[2] Metzger, D. E., Yamashita, T., and Jenkins, C., 1969, "Impingement Cooling of Concave Surfaces With Lines of Circular Air Jets," ASME J. Eng. Gas Turbines Power, **91**(3), pp. 149–155.
[3] Metzger, D., Takeuchi, D., and Kuenstler, P., 1973, "Effectiveness and Heat Transfer With Full-Coverage Film Cooling," ASME J. Eng. Gas Turbines Power, **95**(3), pp. 180–184.
[4] Kercher, D., and Tabakoff, W., 1970, "Heat Transfer by a Square Array of Round Air Jets Impinging Perpendicular to a Flat Surface Including the Effect of Spent Air," ASME J. Eng. Gas Turbines Power, **92**(1), pp. 73–82.
[5] Martin, H., 1977, "Heat and Mass Transfer Between Impinging Gas Jets and Solid Surfaces," *Advances in Heat Transfer*, Vol. 13, Academic Press, New York, pp. 1–60.
[6] Florschuetz, L., Truman, C., and Metzger, D., 1981, "Streamwise Flow and Heat Transfer Distributions for Jet Array Impingement With Crossflow," ASME Paper No. 81-GT-77.
[7] Florschuetz, L., Metzger, D., and Su, C., 1983, "Heat Transfer Characteristics for Jet Array Impingement With Initial Crossflow," ASME Paper No. 83-GT-28.
[8] Behbahani, A., and Goldstein, R., 1983, "Local Heat Transfer to Staggered Arrays of Impinging Circular Air Jets," ASME J. Eng. Gas Turbines Power, **105**(2), pp. 354–360.
[9] Chupp, R. E., Helms, H. E., and McFadden, P. W., 1969, "Evaluation of Internal Heat Transfer Coefficients for Impingement-Cooled Turbine Airfoils," J. Aircr., **6**(3), pp. 203–208.
[10] Metzger, D. E., Baltzer, R., and Jenkins, C., 1972, "Impingement Cooling Performance in Gas Turbine Airfoils Including Effects of Leading Edge Sharpness," ASME J. Eng. Gas Turbines Power, **94**(3), pp. 219–225.
[11] Hrycak, P., 1981, "Heat Transfer From a Row of Impinging Jets to Concave Cylindrical Surfaces," Int. J. Heat Mass Transfer, **24**(3), pp. 407–419.
[12] Bunker, R., and Metzger, D., 1990, "Local Heat Transfer in Internally Cooled Turbine Airfoil Leading Edge Regions: Part II—Impingement Cooling Without Film Coolant Extraction," ASME J. Turbomach., **112**(3), pp. 451–458.
[13] Taslim, M., Pan, Y., and Spring, S., 2001, "An Experimental Study of Impingement on Roughened Airfoil Leading-Edge Walls With Film Holes," ASME Paper No. 2001-GT-0152.
[14] Taslim, M., Bakhtari, K., and Liu, H., 2003, "Experimental and Numerical Investigation of Impingement on a Rib-Roughened Leading-Edge Wall," ASME Paper No. GT2003-38118.
[15] Taslim, M., and Bethka, D., 2009, "Experimental and Numerical Impingement Heat Transfer in an Airfoil Leading-Edge Cooling Channel With Cross-Flow," ASME J. Turbomach., **131**(1), p. 011021.
[16] Elebiary, K., and Taslim, M., 2013, "Experimental/Numerical Crossover Jet Impingement in an Airfoil Leading-Edge Cooling Channel," ASME J. Turbomach., **135**(1), p. 011037.
[17] Andrei, L., Carcasci, C., Da Soghe, R., Facchini, B., Maiuolo, F., Tarchi, L., and Zecchi, S., 2013, "Heat Transfer Measurements in a Leading Edge Geometry With Racetrack Holes and Film Cooling Extraction," ASME J. Turbomach., **135**(3), p. 031020.
[18] Facchini, B., Maiuolo, F., Tarchi, L., and Ohlendorf, N., 2013, "Experimental Investigation on the Heat Transfer in a Turbine Airfoil Leading Edge Region:

Effects of The Wedge Angle and Jet Impingement Geometries," European Turbomachinery Conference (ETC), Lappeenranta, Finland, Apr. 15–19, Paper No. ETC2013-130.
[19] Iacovides, H., Kounadis, D., Launder, B. E., Li, J., and Xu, Z., 2005, "Experimental Study of the Flow and Thermal Development of a Row of Cooling Jets Impinging on a Rotating Concave Surface," ASME J. Turbomach., **127**(1), pp. 222–229.
[20] Craft, T., Iacovides, H., and Mostafa, N., 2008, "Modelling of Three-Dimensional Jet Array Impingement and Heat Transfer on a Concave Surface," Int. J. Heat Fluid Flow, **29**(3), pp. 687–702.
[21] Craft, T. J., Iacovides, H., and Mostafa, N. A., 2008, "Numerical Modelling of Flow and Heat Transfer From an Array of Jets Impinging Onto a Concave Surface Under Stationary and Rotating Conditions," ASME Paper No. GT2008-50624.
[22] Hong, S. K., Lee, D. H., and Cho, H. H., 2008, "Heat/Mass Transfer Measurement on Concave Surface in Rotating Jet Impingement," J. Mech. Sci. Technol., **22**(10), pp. 1952–1958.
[23] Hong, S. K., Lee, D. H., and Cho, H. H., 2009, "Effect of Jet Direction on Heat/Mass Transfer of Rotating Impingement Jet," Appl. Therm. Eng., **29**(14), pp. 2914–2920.
[24] Hong, S. K., Lee, D. H., and Cho, H. H., 2009, "Heat/Mass Transfer in Rotating Impingement/Effusion Cooling With Rib Turbulators," Int. J. Heat Mass Transfer, **52**(13), pp. 3109–3117.
[25] Deng, H., Gu, Z., Zhu, J., and Tao, Z., 2012, "Experiments on Impingement Heat Transfer With Film Extraction Flow on the Leading Edge of Rotating Blades," Int. J. Heat Mass Transfer, **55**(21), pp. 5425–5435.
[26] Jung, E. Y., Park, C. U., Lee, D. H., Park, J. S., Park, S., and Cho, H. H., 2013, "Effect of Rotation on Heat Transfer of a Concave Surface With Array Impingement Jet," ASME Paper No. GT2013-95443.
[27] Bonanni, L., Carcasci, C., Facchini, B., and Tarchi, L., 2012, "Experimental Survey on Heat Transfer in a Trailing Edge Cooling System: Effects of Rotation in Internal Cooling Ducts," ASME Paper No. GT2012-69638.
[28] Chan, T., Ashforth-Frost, S., and Jambunathan, K., 2001, "Calibrating for Viewing Angle Effect During Heat Transfer Measurements on a Curved Surface," Int. J. Heat Mass Transfer, **44**(12), pp. 2209–2223.
[29] Bianchini, C., Burberi, E., Cocchi, L., Facchini, B., Massini, D., and Pievaroli, M., 2015, "Numerical Analysis and Preliminary Experimental Heat Transfer Measurements on a Novel Rotating Leading Edge Model," 12th International Symposium on Experimental Computational Aerothermodynamics of Internal Flows, Genova, Italy, July 13–16.
[30] Willert, C., 1997, "Stereoscopic Digital Particle Image Velocimetry for Application in Wind Tunnel Flows," Meas. Sci. Technol., **8**(12), pp. 1465–1479.
[31] Furlani, L., Armellini, A., Casarsa, L., 2017, "Effects of Rotation and Buoyancy Forces on the Flow Field Behavior Inside a Triangular Rib Roughened Channel," ASME. J. Turbomach., **139**(5), p. 051001.
[32] Armellini, A., Mucignat, C., Casarsa, L., and Giannattasio, P., 2012, "Flow Field Investigations in Rotating Facilities by Means of Stationary PIV Systems," Meas. Sci. Technol., **23**(2), p. 025302.
[33] Furlani, L., Armellini, A., Casarsa, L., 2016, "Rotational Effects on the Flow Field Inside a Leading Edge Impingement Cooling Passage," Exp. Therm. Fluid Sci., **76**, pp. 57–66.
[34] ASME, 1985, "Measurement Uncertainty in Instrument and Apparatus," ASME, New York, Standard No. ANSI/ASME PTC 19.1-1985 of Performance Test Code.
[35] Kline, S. J., and McClintock, F. A., 1953, "Describing Uncertainties in Single Sample Experiments," Mech. Eng., **75**(1), pp. 3–8.
[36] Armellini, A., Casarsa, L., and Giannattasio, P., 2009, "Separated Flow Structures Around a Cylindrical Obstacle in a Narrow Channel," Exp. Therm. Fluid Sci., **33**(4), pp. 604–619.
[37] Andreini, A., Burberi, E., Cocchi, L., Facchini, B., Massini, D., and Pievaroli, M., 2015, "Heat Transfer Investigation on an Internal Cooling System of a Gas Turbine Leading Edge Model," Energy Procedia, **82**, pp. 222–229.
[38] Burberi, E., Massini, D., Cocchi, L., Mazzei, L., Andreini, A., and Facchini, B., 2017, "Effect of Rotation on a Gas Turbine Blade Internal Cooling System: Numerical Investigation," ASME J. Turbomach., **139**(3), p. 031005.